INVESTIGATION OF SEVERAL TERAHERTZ ELECTROMAGNETIC BAND GAP STRUCTURES

Ziran Wu,[1,2] Abram Young,[2] Michael Gehm,[1] and Hao Xin[1,2]
[1] Department of Electrical and Computer Engineering, University of Arizona, Tucson, AZ; Corresponding author: hxin@ece.arizona.edu
[2] Department of Physics, University of Arizona, Tucson, AZ

Received 17 August 2009

ABSTRACT: *Several THz electromagnetic band gap (EBG) structures are investigated and demonstrated. Various design, fabrication, and characterization methods and techniques are utilized and compared. These THz EBG structures may enable future high performance EBG based THz components.* © 2010 Wiley Periodicals, Inc. Microwave Opt Technol Lett 52: 678–686, 2010; Published online in Wiley InterScience (www.interscience.wiley.com). DOI 10.1002/mop.24986

Key words: *THz; electromagnetic band gap; rapid prototyping*

1. INTRODUCTION

Research involving Terahertz (THz) spectrum spanning from 100 GHz to 10 THz [1] has enjoyed dramatic growth in terms of technical achievements as well as commercial implementations in recent years [2]. This growth is application driven with interests from widely ranged fields such as chemical and astronomic spectroscopy and sensing [2], medical and biological imaging and analysis [3], defense and security screening, material research and semiconductor industry [4], next generation communication networks and radars [5], etc. The great potential of THz technology originates from the plethora of physical and chemical processes occurring in this region and the high resolution and bandwidth of THz compared with microwave frequencies. In addition, free space THz propagation suffers less scattering loss than free space propagation of IR and visible light so that THz systems are able to function under IR and visible blind conditions such as smoke, cloud, and sand storm. Many THz applications have become closer to reality with the advancement of new THz sources, detectors, and other components.

As the first demonstration in the late 80s, electromagnetic (or "photonic" for optical spectra) crystals have been one of the most active research areas in microwave and optical engineering. In analogy to semiconductor crystals [6], electromagnetic crystals can be used to manipulate the flow of electromagnetic waves due to the multiple scattering from their periodic dielectric and metallic structures. One basic phenomenon is the prohibition of electromagnetic wave propagation in certain direction, or total forbiddance of propagation in any direction within certain frequency band, thus the name electromagnetic band gap (EBG). A multitude of applications such as antennas, filters and wave guiding devices [5], microlasers [7], ultrafast switches [8], and spontaneous emission control [9] from microwave to optical frequencies have been proposed and investigated.

The introduction of EBG into THz region is first motivated by THz wave guiding in THz spectroscopy. Free space THz propagation devices can be bulky, expensive, and inflexible for many applications, for example, a sample under study may not always be accessible by a free space beam. Conventional waveguides have limitations on THz beam guiding due to their high loss and high dispersion, which results in severe THz pulse reshaping and attenuation problems [1]. THz waveguides based on EBG structures are able to guide THz beam efficiently with advantages of having better confinement, smaller size, low dispersion and low loss. Continuous efforts have been paid on EBG based THz components, among them, sources, detectors, filters, and waveguides [2, 5, 10]. However, the realization of THz EBG components still faces some challenging issues including efficient design and fabrication processes and accurate characterization methods. In this article, we present the design, fabrication, and characterization of several dielectric and metallic THz EBG structures with 1D, 2D, and 3D periodicity. Several EM calculation techniques are applied to aid the design of these structures, with their respective advantages compared. Different structures involve different fabrication techniques, among which the most challenging three-dimensional fabrication has been greatly simplified by a THz rapid prototyping technique based on polymer jetting. Three commonly used THz instruments based on distinct physical principles, including THz time domain spectroscopy (THz-TDS), far-infrared Fourier transform spectroscopy (FIR-FTS) and vector network analyzer (VNA), are utilized for sample characterization. Features of each instrument are discussed and a common 3D EBG sample is measured as a bench mark comparison for all three instruments. This work demonstrates useful building blocks and provides practical design, fabrication and characterization guidelines for THz EBG structures which may enable future high performance EBG based THz components.

As a revision to the original APMC2008 conference proceeding [11], this article expands the original paper into complete sections detailing the design, fabrication, and characterization processes of

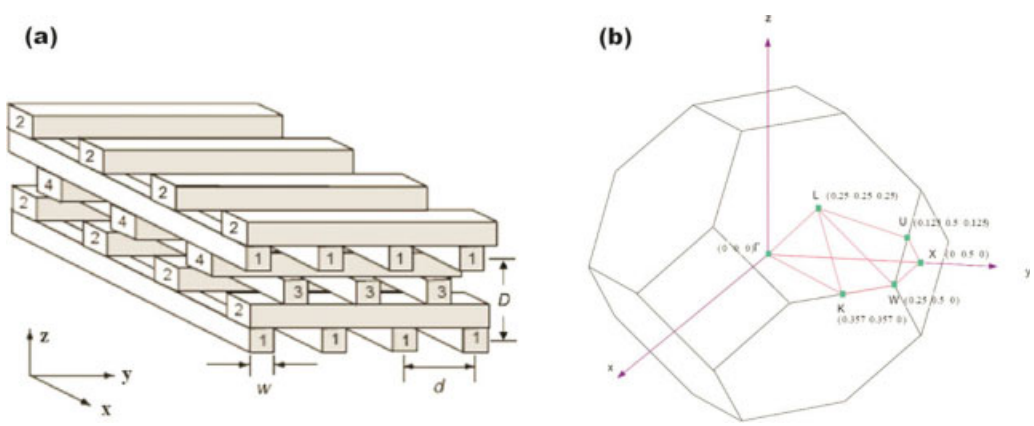

Figure 1 (a) Schematic of the WPS structure [12]. (b) The first BZ of the WPS face-center-tetrahedron (fct) lattice, with apex of its irreducible BZ (characteristic k-points) marked. [Color figure can be viewed in the online issue, which is available at www.interscience.wiley.com]

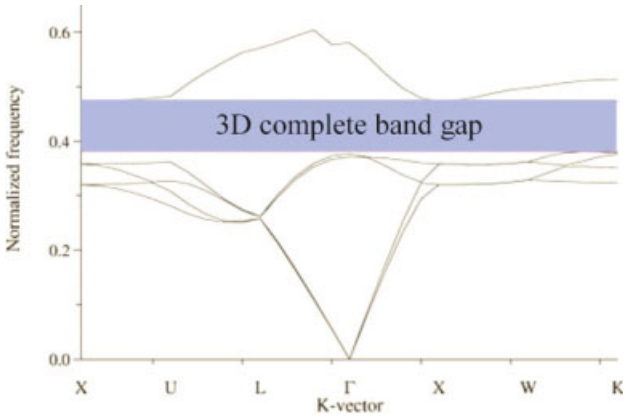

Figure 2 Calculated band diagram of the silicon WPS. The 3D complete band gap is indicated by the shaded region. [Color figure can be viewed in the online issue, which is available at www.interscience.wiley.com]

several THz EBG building blocks. Different testing methodologies with focuses on comparing their features are described. In addition, a new THz rapid prototyping technique is included with examples.

2. DESIGN

2.1. Band Diagram Calculation

It is useful to start with the band diagram when designing a THz EBG structure. For a structure with a periodic lattice, the band diagram calculation is done within its reciprocal lattice space, or, the *k*-vector space. Irreducible Brillouin zone (BZ), as the smallest unit cell reduced by all of the symmetries in the reciprocal space, describes the entire dispersion relation of the structure. Moreover, the edges of the irreducible BZ define the upper and lower boundaries of each energy band. Eigen-energy calculation is therefore carried out along the edges to map out the band diagram of an EBG structure.

A schematic of the well-known woodpile structure (WPS) is illustrated in Figure 1(a) [12]. It has a unit cell of four layers of infinite long square rods made of high refractive index material, hereby assigned as silicon ($n = 3.6$). The rods are stacked in the *z*-direction with a periodicity *D*. Each adjacent layers with the same rods orientation (*x* or *y* direction) are shifted relative to each other by half of the periodicity *d* within one layer. Each rod has a width *w* and a height *D*/4. The background low refractive index material is usually air ($n = 1.0$). Alternatively, the WPS can be decomposed into unit cells made of any two rods perpendicular to each other (such as any pair of rod 1 and 2 in Fig. 1) which are repeated in a face-centered-tetragonal (fct) lattice over space. Also shown in Figure 1(b) is the first BZ of the WPS fct lattice, with the first irreducible BZ and the characteristic points *L*, *U*, *X*, *W*, *K*, Γ (apex of the first irreducible BZ) marked. The eigen-energy calculation is done with the MIT Photonic-Bands (MPB) package based on plane wave basis expansion method [13]. The resulting WPS band diagram is shown in Figure 2. It can be seen that between the normalized frequencies (the normalized frequency *x* relates to the real frequency *f* as follows, $f = c_0x/a$, where c_0 is the speed of light and *a* is the lattice constant) 0.38 and 0.47, there is a blank region without any eigen-mode existing. Therefore, the WPS exhibits a complete 3D band gap in that frequency range. Because of the large band gap width (with a gap/mid-gap ratio of 21.49%) of this design, it can be very useful in the applications of antenna substrate [5], waveguides [14], filter [15] and THz thermal radiation source [10].

As verification, the WPS band diagram is also calculated using the commercial 3D finite-element (FEM) electromagnetic solver Ansoft HFSS [16]. In this case, a simple-tetragonal (st) unit cell consists of two of the previous fct unit cells is used. With appropriate periodic (Master/Slave in HFSS) boundary condition settings, specific *k*-vectors in the reciprocal lattice space can be swept. Good agreement is obtained between the HFSS and MPB eigen-mode results [10]. Although much more computationally intensive in terms of both CPU and memory requirements, the main benefit of calculating eigen-modes with HFSS is that it can handle materials with arbitrary loss and dispersion, whereas in MPB, only lossless dielectrics can be included. However, spurious mode may be present in HFSS calculation, especially for highly resonant structures.

Another option for calculating the band diagram is to use the MIT electromagnetic equation propagation (MEEP) package [17] based on the finite-difference-time-domain (FDTD) method. In this case, resonance modes of an EBG structure are found by identifying sinusoids having sufficient long life-time after the excitation pulse is turned off. One advantage of the MEEP eigen-mode solver over MPB is that the radiation boundary is built in. Therefore, resonant modes of open structures, such as EBG structures with finite size or arbitrary defects, can be simulated. In addition, MEEP allows lossy dielectric and metallic structures to be calculated.

A 2D metallic wire array EBG structure, as shown in Figure 3(a), is studied using MEEP. Metallic wires with radius *r* are

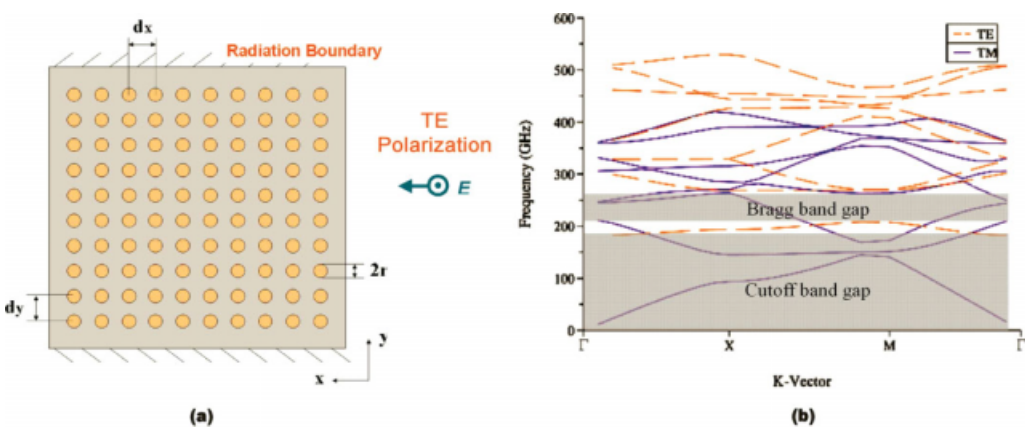

Figure 3 (a) Top view of a 2D metallic wire array. (b) Wire array band diagram, dashed red line for TE polarization, solid blue line for TM polarization. [Color figure can be viewed in the online issue, which is available at www.interscience.wiley.com]

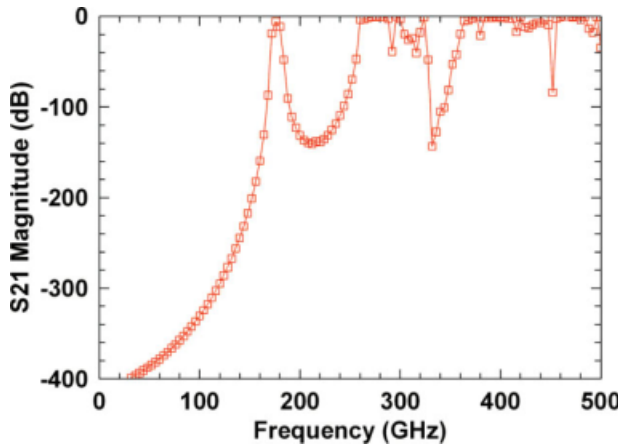

Figure 4 HFSS simulated transmission response of the 2D wire array. [Color figure can be viewed in the online issue, which is available at www.interscience.wiley.com]

arranged in a simple-cubic lattice to form the array. The dimensions are, $dx = dy = 1.168$ mm and $r = 0.304$ mm. One interesting application of the wire array EBG structure is that negative or near-zero effective permittivity can be achieved below or at a cutoff frequency (sometimes called plasma frequency) due to the reduction of electron density and the enhancement of electron effective mass through self-induction between wires [18]. In addition, this structure also exhibits EM band gap properties at higher frequencies when the wire spacing approaches half wavelength, as Bragg diffractions within the wires come into play. The plot in Figure 3(b) shows the band diagrams for two independent polarizations, TE for the E-field along the z direction, and TM for the E-field along the y direction. For the TE case, there are no eigen-modes existing below 180 GHz, indicating the cutoff frequency. Moreover, a Bragg band gap is apparent between 200 and 260 GHz for the TE case. There are no band gaps existing for the TM case.

2.2. Transmission Response Verification

Once the dimensions of a THz EBG structure are obtained from the calculated band diagram, the design can be verified by finite-element simulation of the transmission response of the actual model. Figure 4 plots the simulated transmission response of the same 2D wire array structure shown in Figure 3. The simulated transmission response reveals the cutoff frequency at 180 GHz as well as the Bragg band gap centered near 230 GHz, agreeing well with the band diagram results.

An alternative approach to obtain the transmission response is the transfer matrix method (TMM) [19]. TMM treats each cascaded section of a structure separately and solves Maxwell's equations to obtain the scattering matrix of each section. By successive multiplication of each scattering matrix, the reflection and transmission coefficients of the overall structure can be calculated [5]. An example of a 1D silicon/air bi-layer EBG structure is shown in Figure 5.

The unit cell of the 1D EBG structure consists of one layer of silicon and one layer of air, with thickness a and b, respectively. The high contrast of refractive indices between silicon and air leads to the prohibition of wave propagation at certain frequencies through destructive Bragg diffraction, even though silicon and air themselves are transparent to the EM waves. The dimensions used here are, $a = 350$ μm and $b = 1220$ μm. Figure 5(b) plots the calculated transmission coefficient using TMM. This 1D bi-layer structure has periodic band pass and band stop responses every 114 GHz, making it suitable for broadband and multi-band filtering applications.

3. FABRICATION

3.1. Conventional Fabrication Methods

Despite the advancements of THz EBG components and applications, one of the major challenges remaining to be overcome involves the practical difficulties in component fabrication (especially at integrated micro-system level), as the feature dimensions of THz EBG components fall in a transition region between the conventional machining techniques used for microwave applications and the micro/nano fabrication methods in use at optical frequencies [20]. Several semiconductor fabrication approaches for THz components, including dicing saw machining [21], wet etching [22], deep reactive iron etching (DRIE) [23], deep X-ray lithography [24] and laser micromachining [20, 24], have been reported. These methods are usually expensive, and require extraordinary care to achieve even relatively uniform THz EBG geometries, let alone the more complicated structures such as defect cavities and waveguides.

A 3D WPS designed based on the band diagram shown in Figure 2 is fabricated by the mechanical layer-by-layer dicing saw machining method [21]. The WPS dimensions are designed to be the following to achieve a band gap frequency of around 200 GHz: rod width $w = 176$ μm, rod spacing $d = 646$ μm and unit cell height $D = 704$ μm [see Fig. 1(a)]. High resistivity silicon (bulk conductivity 0.01 Siemens/m) is used as the building material. The dicing and assembly processes are illustrated in Figure 6. A series of grooves are cut into both the front and back sides of a silicon substrate (the front and back orientations are rotated by 90°) by using a programmable diamond dicing saw. The depth of the cut is set so as to open a window at the crossing point of the cuts, but leaving the array joined at the crossing points of the resulting bars. Each substrate makes up one half of the WPS unit cell in Figure 1(a). The complete WPS

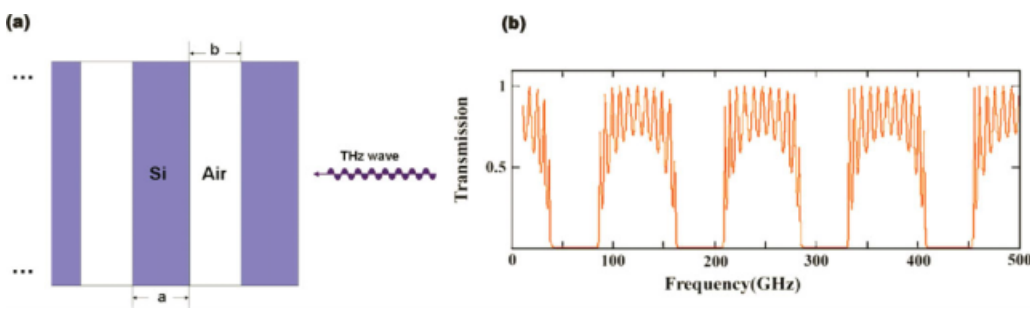

Figure 5 (a) Schematic of a 1D silicon/air slab EBG structure. (b) Transfer matrix method predicted transmission spectrum. [Color figure can be viewed in the online issue, which is available at www.interscience.wiley.com]

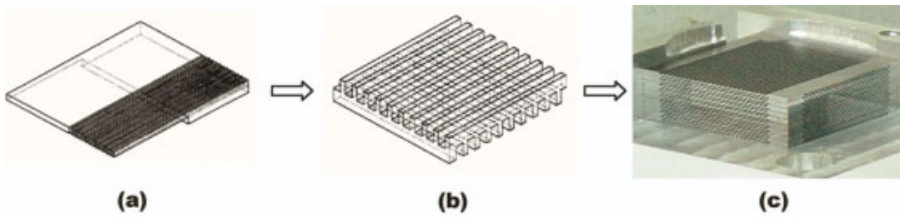

Figure 6 Illustration of the fabrication process for a 9-unit cell silicon WPS. [Color figure can be viewed in the online issue, which is available at www.interscience.wiley.com]

is then assembled by stacking many substrates together with the help of pre-registered alignment marks. A picture of the fabricated woodpile structure is shown in Figure 6(c), with a total of 9 unit cells in the stacking direction.

3.2. Polymer-jetting Rapid Prototyping

Although the aforementioned dicing process is relatively simple, the fabrication of a THz structure still requires significant skills and is time intensive. In addition, accurate alignment and assembly of the diced silicon pieces can be challenging. Alternatively, a variety of rapid prototyping technologies have been explored for fabricating 3D microwave circuits and EBG components, including polymer and ceramic stereolithography [25, 26], fused deposition modeling [27] and selective laser sintering [27]. Among them, polymer stereolithography has the highest accuracy [26]. Using these methods, EBG waveguides [28], 3D antennas [29] and band-pass filters [25] have been demonstrated. However, these techniques were only successful at frequencies up to ~30 GHz. Recently, a rapid and inexpensive polymer-jetting technique for high-quality THz EBG structure fabrication has been demonstrated by our group [30]. Besides the low cost and fast speed of this technique, the most noticeable advantage is its ability of achieving high geometry flexibility.

Polymer-jetting rapid prototyping machines that are traditionally used in mechanical engineering now have build resolutions that fall in the range of THz wavelengths. The polymer-jetting printer used in this work states a resolution of 42 μm $\times$ 42 μm $\times$ 16 μm, which is sufficient for fabrication of EBG components with THz features. Moreover, large structures with a footprint of up to 30 cm $\times$ 30 cm can be printed so that batch fabrication of a large number of THz components is possible. In the fabrication, the 3D geometry of a THz EBG component is exported into a CAD program where it is converted into a series of layered slices, each representing a 16-μm thick region of the model. As earlier slices provide the surface upon which later slices are constructed, the slice description consists of two different material types-a model material which is assigned to regions that are actually part of the cross-section of the desired object, and a support material, which is used to provide a base upon which the model sections of future slices can rest. The data describing the slices are sent sequentially to the prototyping machine. A series of print heads, much like the print heads of an inkjet printer, deposit a thin layer of UV-curable polymer onto the construction tray. Regions identified as model material in the slice are covered with uncured acrylic polymer, while support material regions receive uncured water-soluble polymer. UV lamps on the print head immediately cure both materials as they are being deposited. After the layer is complete, the construction tray is lowered by 16 μm and the next slice is processed. After the entire model is printed, the construction tray rises and the part may be removed. The finishing step involves using a high-pressure water spray to remove the water-soluble support material, leaving just the model material in the desired 3D shape.

Our initial attempt with the polymer-jetting prototyping technique involves a similar WPS with a band gap near 200 GHz. The printed polymer WPS sample has 5 unit cells in the stacking direction and a 6 cm $\times$ 6 cm sample area, as shown in Figure 7. In the cross-section view, clean and sharp feature edges are clearly seen. The build time of the sample is ~30 min with consumable costs of less than $10, and no alignment procedure is necessary after the construction.

A more complicated 3D EBG structure explored is first proposed by Johnson and Joannopoulos [31], and later fabricated by the same group [32] using semiconductor approaches. We refer to this structure as the "Johnson-structure" (JS). A computer rendered structure model is shown in Figure 8(a) (left). The structure consists of two alternating 2D triangular lattice layers, one being pseudo-hexagonal dielectric pillars standing in air background (rod layer), and the other being air holes in dielectric background (hole layer). Each air hole has a radius r, and the geometry of each dielectric pillar is determined by the three surrounding air holes. Both the rod and hole layers have the same lattice constant x. Two adjacent rod layers or hole layers are shifted from each other by $x\sqrt{3}$ in the x direction, thus forming the ABCA sequence in the stacking z direction, as shown in Figure 8(a) (lower right). The structure's unit cell therefore includes three rod layers and three hole layers along the stacking direction. Figure 8(a) (upper right) shows the structure's cross section: the height of the through air holes is h, and the height of two touching layers (one hole layer and one rod layer) is t.

The fabrication of the JS would be very complicated with other approaches. However, it can be easily done by the polymer-jetting prototyping technique due to its layer-by-layer construction nature. The fabricated THz JS has the following dimensions: triangular lattice constant $x = 1346$ μm, air hole radius $r = 500$ μm, air hole height $h = 1713$ μm, and rod/hole layer height $t = 1071$ μm. A photograph of the fabricated JS is shown in Figure 8(b) (left). A top and a side microscopic view of the sample are also included in Figure 8(b) (right). In the top view (lower right), the hexagonal air

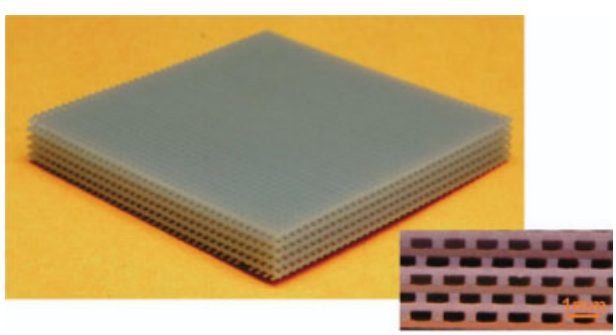

Figure 7 Photograph of the fabricated polymer THz WPS. Inset is a zoomed-in view of the sample cross-section. [Color figure can be viewed in the online issue, which is available at www.interscience.wiley.com]

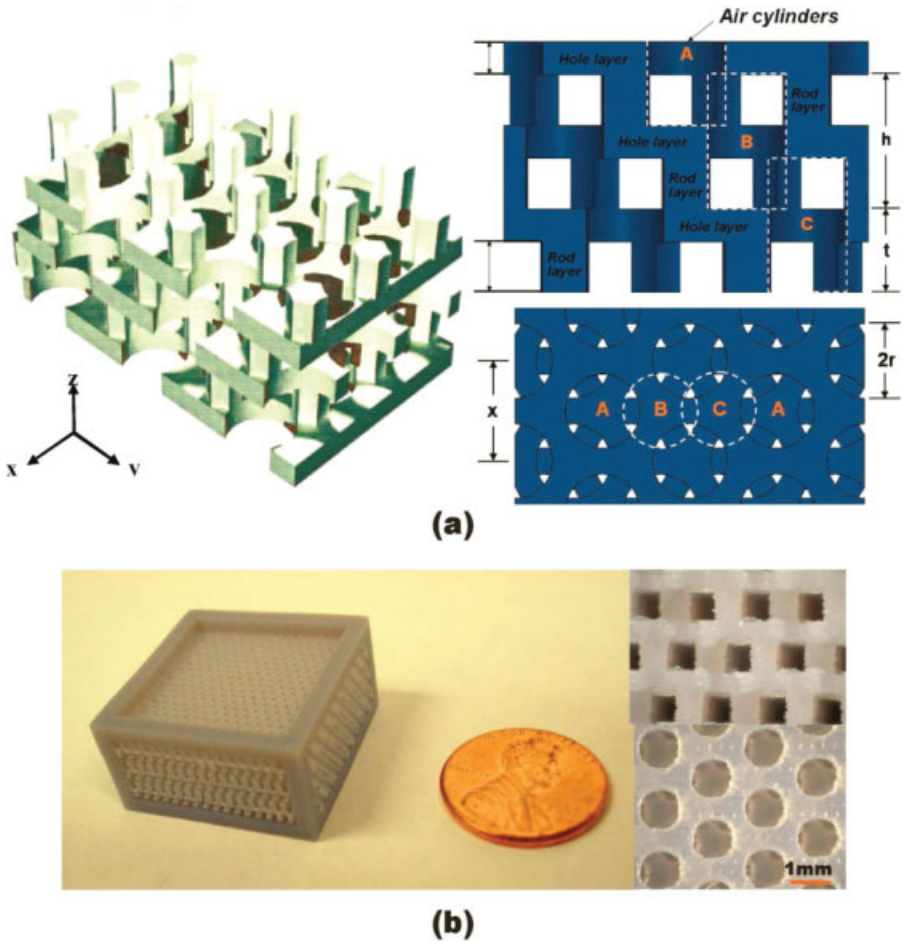

Figure 8 (a) Schematics of a Johnson EBG structure, including: a 3D model (left) showing one unit cell in the stacking direction and several periods in horizontal (from [31]), the cross-sectional view (upper right), and the top view (lower right). (b) Photographs of the fabricated polymer JS, including: the full view (left), the side view (upper right), and the top view (lower right). Reprinted with permission from Johnson SG, Joannopoulos JD, Appl Phys Lett 77, 22, 3490–3492, 2000. © 2000 American Institute of Physics. [Color figure can be viewed in the online issue, which is available at www.interscience.wiley.com.]

hole array is clearly defined, and the shifted hole layers underneath can be seen. A design choice results in the posts having truly circular cross-sections, but this is not expected to dramatically impact the EM behavior of the structure [31]. The shifted adjacent rod layers are also correctly fabricated, as can be seen in the side view. Three unit cells consisting of 9 hole layers and 9 rod layers are fabricated, resulting in an overall EBG structure dimension of 25 mm $\times$ 25 mm $\times$ 9.6 mm.

Because of the rapid build process, low cost and the arbitrary geometry flexibility, this prototyping technique may enable fabrication of complete THz micro-systems. For example, an integrated THz waveguides, filters, antennas and even transition parts to planar devices and circuits may be fabricated simultaneously, without post processing and assembling. Although currently the polymer-jetting technique only prints dielectric build materials with a fixed index of refraction, it is conceivable that in the near future, conducting polymers and materials with different dielectric constants may be mixed to allow the realization of 3D structures with arbitrarily distributed electromagnetic properties.

4. CHARACTERIZATION

4.1. THz Characterization Instruments

THz characterization of a sample is usually done by measuring the transmission or reflection responses of a probing signal. It has been a great technical challenge due to the relatively low photon energy and the lack of efficient THz components. The former condition implies a vast amount of noise and thus poor signal-to-noise ratio (SNR) originating from the ambient background thermal radiation. The latter situation includes the lack of efficient THz sources, detectors and wave guiding components. Currently available THz sources are usually expensive and limited to low power output. THz spectra are occupied by many molecular vibration lines, which hinder THz spectral characterization too.

Most commonly used and commercially available THz characterization instruments include THz time domain spectrometer (THz-TDS), far-infrared Fourier transform spectrometer (FIR-FTS), and vector network analyzer (VNA). Other THz instruments include THz radiometer, ellipsometer and confocal microscope, but not as widely used. The transmission measurement setups of THz-TDS and FIR-FTS are illustrated in Figure 9.

A typical THz-TDS includes a femtosecond laser, a beam splitter, a pair of THz emitter and receiver, collimating optics, an optical delay stage, and data acquisition system [see Fig. 9(a)]. The emitter utilizes either photoconductive antenna based on free electron radiation, or electro-optical crystal based on optical rectification, to generate THz signal. The detector of a THz-TDS is capable to record picosecond-duration pulse waveform via ultra-fast gating and sampling system [33]. The measured waveform is Fourier transformed to extract the spectrum. In a transmission configuration the sample is placed in and out

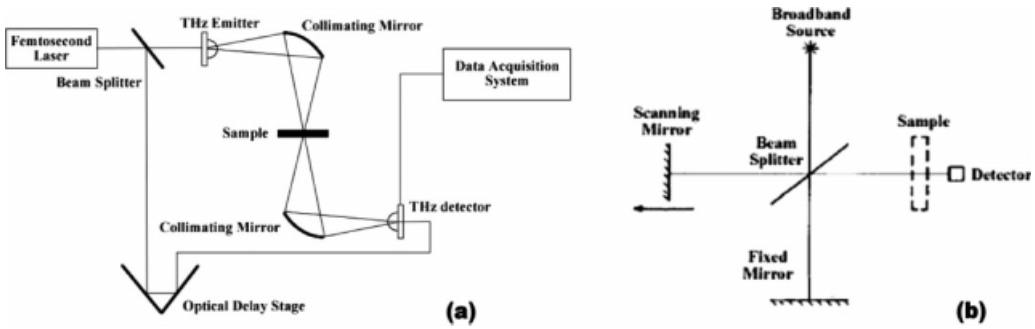

Figure 9 (a) THz-TDS experiment setup. (b) FIR-FTS block diagram

of the THz beam path, and comparison of the two spectra provides the transmission characteristics of the sample.

A far-IR FTS, on the other hand, consists of a broadband high-pressure mercury arc lamp as the source, a beam splitter, one fixed mirror and one scanning mirror, a power detector, and data acquisition system [see Fig. 9(b)]. Path difference between the scanning and fixed mirrors brings in a phase delay between the two split beams. Different frequency components in the beam experience different phase delays and interfere accordingly. Therefore, these components are amplitude-modulated and recorded as an interferogram, whose modulation frequencies are directly scaled-down frequencies from the original signal [10]. The spectrum of the signal is then recovered by Fourier transformation of the interferogram. Similar to the THz-TDS, two scans with sample in and out of the beam path are sufficient to characterize the sample transmission response.

VNA consists of a frequency-tunable THz source, two-channel transmitter and receiver, phase detection unit and data acquisition systems. Incident wave with very narrow bandwidth—approximately monochromatic—passes through the sample via waveguide or free space coupling. Reflected and transmitted signals are recorded, and by calibration procedures they can be de-embedded to the sample surfaces. Reflectance and transmittance of the sample are obtained with both magnitude and phase. Time domain response of the sample may also be obtained by real-time inverse Fourier transform of the detected frequency-domain signal.

Each of these three characterization instruments has its own advantages and disadvantages. Table 1 compares some of the main characteristics of these instruments [34].

Transmission and reflection setups are available for all three instruments; however both measurements can be done simultaneously by a VNA without the necessity of rearranging the equipment. Phase measurement is readily available for THz-TDS and VNA, whereas FIR-FTS cannot measure phase directly because it uses a power detector such as bolometer or Golay cell; however, the phase delay introduced by a sample is measurable if the sample is placed between the beam splitter and either scanning or fixed mirror [see Fig. 9(b)] [34]. In that case, sample in and out result in two different interference intensities when the mirrors are at the same positions. By comparing the phase difference of the Fourier transformed interferograms the extra phase delay due to the sample can be obtained. For the spectral specifications, THz-TDS has a fairly good dynamic range over a wide bandwidth, because its unique gating system excludes most of the background radiation. Frequency resolution of the VNA is the best so that it is capable of resolving very fine spectral lines. However, its overall measurement bandwidth is limited comparing with the other two instruments. Also, different transmitter/detector modules and calibration kits are necessary to cover different frequency ranges.

4.2. Characterization Results

Transmission responses of all the 1D, 2D, and 3D EBG structures are characterized to validate the design and fabrication procedures. For brevity, only the results of the 3D structures are included here. To compare the three instruments discussed in the previous section and obtain independent confirmation of the results, the silicon WPS as shown in Figure 6 is characterized by all three instruments. The THz-TDS system used is a commercially available T-ray 2000 with photoconductive antenna emitter and detector. The system covers from around 50 GHz to 1.2 THz. The FIR-FTS used is a Beckman FS-720 step-scan Michelson interferometer with liquid Helium cooled bolometer as detector to cover from 150 GHz to 3 THz. The VNA measurement is done with an Agilent PNA E836x network analyzer

TABLE 1 Specification Comparisons of THz-TDS, FIR-FTS, and VNA

	THz-TDS	Far-IR FTS	VNA
Measure. domain	Time domain	Frequency domain	Frequency domain
Transmission/reflection	Both available	Both available	Measured simultaneously
Phase measurement	Available	Need special setup	Available
Dynamic range of power	1e8 (<3 THz)	~300 (<3THz)	1e19 at 200 GHz 1e6 at 700 GHz
Typical resolution	3 GHz	3 GHz	10 KHz
Peak power	1 mW (integrate over the bandwidth)	0.1 uW (integrate over the bandwidth)	1.3 mW at 200 GHz 0.001 mW at 600 GHz
Bandwidth	Tens of 10 GHz to 45 THz	100 GHz to visible	Up to 1 THz
Noise equivalent power	1*e*-16 W/rtHZ (<3 THz)	8*e*-10 W/rtHZ (<3 THz)	1*e*-12 W/rtHZ min
Source stability	Good	Not good	Good
Setup difficulty	Initial stages	Mature, easy	Initial stages

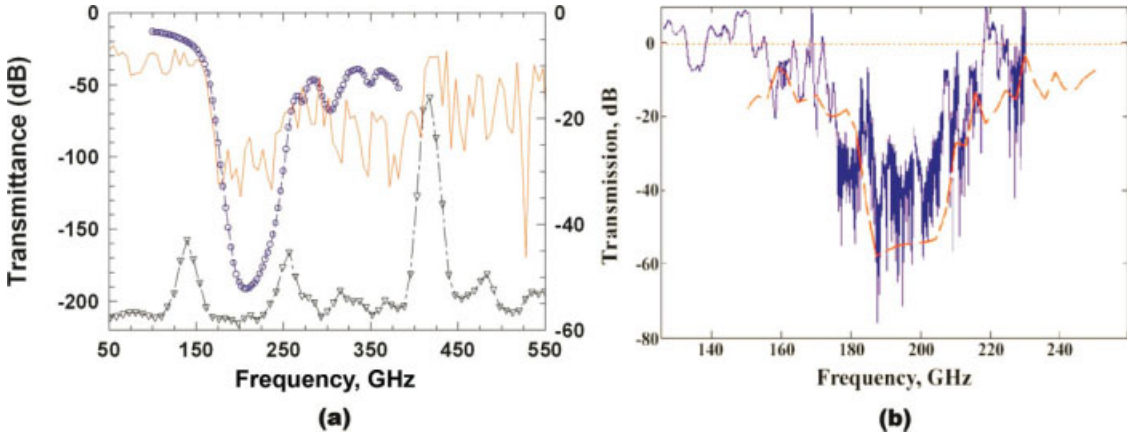

Figure 10 Silicon WPS transmittance: (a) FIR-FTS result (dash-doted line with triangles, a.u.) compared with THz-TDS measurement (solid line, right ordinate) and HFSS simulation (dashed line with circles, left ordinate) results. (b) VNA measurement (solid line) compared with TMM calculation (dashed line). [Color figure can be viewed in the online issue, which is available at www.interscience.wiley.com]

equipped with N5260A mm Wave controller and Oleson frequency extension modules WR-5, WR-6, and WR-8. The best frequency resolution is 1.8 GHz for the THz-TDS, 4.5 GHz for the FTS and 1 KHz for the VNA. Normal incidence is applied, with the incoming wave along the stacking direction of the WPS sample.

In Figure 10(a), THz-TDS (right ordinate) and FTS characterization results are plotted together with the HFSS simulated transmittance. The FTS transmission spectrum is vertically shifted for a clearer view. For normal incidence, simulation predicts the WPS band gap spanning from 180 to 250 GHz. Both the TDS and FTS spectra verify that with very good agreement. Pass-bands from 100 to 160 GHz and around 270 GHz are also observed in both measurements and in good agreement with the simulation. Correspondence with the second band gap at 300 GHz can also be found in both measurements. In general, the sensitivity of the FTS is poor due to low power content at the low frequency end of the mercury lamp source. In addition, the amplitude modulation from the beam splitter can also cause spurious peaks (for example, near 420 GHz).

Figure 10(b) shows the VNA characterization result (solid line) and as a comparison, calculation result using TMM is also plotted. The fundamental band gap around 200 GHz is again verified and good agreement between simulation and experimental results is observed. Due to uncertainties in the calibration procedure, the VNA measured transmittance goes beyond 0 dB at places. Overall, all three measurements are reasonably consistent in the WPS band gap characterization, thus verifying the WPS design and fabrication procedures. Furthermore, from the experimental procedure and results, it is concluded that the THz-TDS is probably the most convenient instrument with sufficient accuracy for our purpose.

To verify that the WPS EBG centered at 200 GHz is a complete 3D band gap independent of polarization, additional THz-TDS measurements are also done with various sample orientations. The presence of the band gap at 200 GHz is always observed (results not shown).

To validate the THz prototyping technique we proposed, the fabricated polymer THz EBG structures are also characterized by the THz-TDS transmission measurement. The results are shown in Figure 11, in comparison with HFSS simulations [30].

The measured and simulated WPS transmittances are in excellent agreement. Not only is the fundamental band gap (centered at 185 GHz) verified, but a small resonance feature near 202 GHz within the band gap can also be consistently seen in both results. Moreover, the simulated and measured secondary

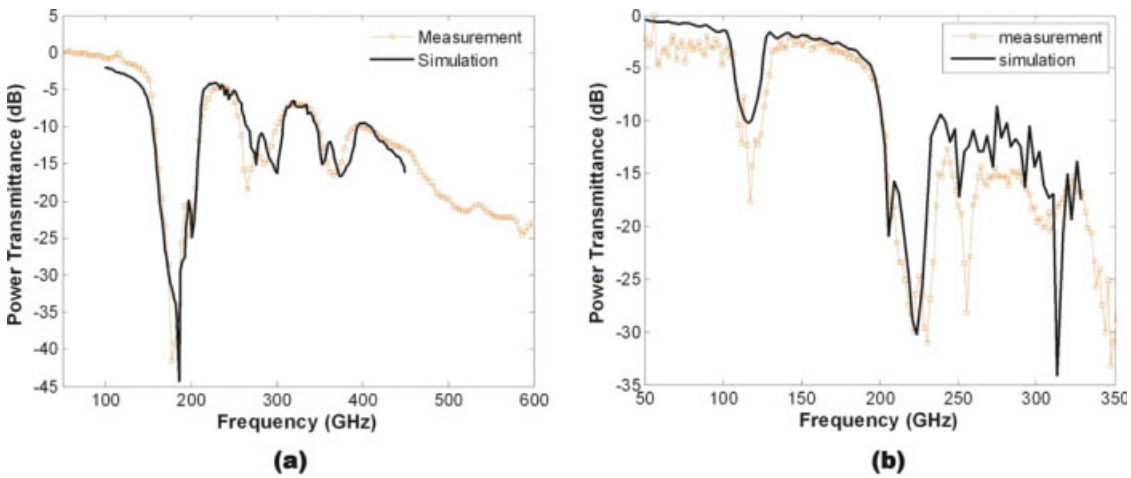

Figure 11 The measured (open squares) and simulated (solid line) normal-incidence power transmittances for (a) the polymer WPS and (b) the polymer JS. [Color figure can be viewed in the online issue, which is available at www.interscience.wiley.com]

and tertiary band gaps (centered at 278 and 372 GHz, respectively) are in very good agreement in terms of location, width and depth. The small (<2 dB) discrepancy of the transmission level at the low frequency end is a result of the overestimation of the material loss in the simulation, because a constant loss tangent of 0.06 for the polymer is assigned in the simulation over the entire frequency range, while the actual loss tangent of the polymer is smaller than that value at low frequencies (verified by measurements [30]).

Characterization of the polymer JS also yields very good agreement with the simulation result. As seen in Figure 11(b), both the mid-gap frequency and the gap rejection depth of the fundamental EBG around 220 GHz are verified. The secondary transmission dip around 120 GHz is also confirmed. Both gaps are slightly wider in the measurement than in the simulation, probably as a result of a small inhomogeneity of the array pitch. The two additional transmission dips measured at 255 and 309 GHz can also be matched to features in the simulated spectrum. The overall excellent agreement between the JS design prediction and the characterization result is significant as it confirms the fabrication accuracy of the polymer jetting technique as well as its capability of realizing complicated THz structures.

5. CONCLUSIONS

This work demonstrates useful building blocks and provides practical design, fabrication, and characterization guidelines for THz EBG structures which may enable future high performance EBG-based THz components. In the design aspect, several computation tools are utilized to calculate the EBG structure band diagrams. Transmission simulations are performed to verify the designed band gap. Conventional micro-fabrication approaches for THz components are summarized and an example of a micro-machined 3D silicon WPS is reported. As a promising solution to the fabrication challenges of THz components, a rapid prototyping method based on polymer jetting is proposed and demonstrated. In the characterization of the THz EBG structures, three commonly used THz instruments are utilized. Important features and specifications of these instruments are compared and discussed. Consistent measurement results of a 3D silicon WPS using all three characterization methods are demonstrated.

REFERENCES

1. K.L. Wang and D.M. Mittleman, Guided propagation of terahertz pulses on metal wires, J Opt Soc B 22 (2005), 2001–2008.
2. P.H. Siegel, Terahertz technology, IEEE Trans Microwave Theory Tech 50 (2002), 910–928.
3. P.H. Siegel, Terahertz technology in biology and medicine, IEEE Trans Microwave Theory Tech 52 (2004), 2438–2447.
4. B. Ferguson and X.C. Zhang, Material for Terahertz science and technology, Nat Mater 1 (2002), 26–33.
5. P. de Maagt, R. Gonzalo, Y.C. Vardaxoglou, and J.-M. Baracco, Electromagnetic band gap antennas and components for microwave and (sub) millimeter wave applications, IEEE Trans Antennas Propag 51 (2003), 2667–2677.
6. T.F. Krauss and R.M. De la Rue, Photonic crystals in the optical regime—Past, present and future, Prog Quant Electron 23 (1999), 51–96.
7. O. Painter, R.K. Lee, A. Scherer, A. Yariv, J.D. O'Brien, P.D. Dapkus, and I. Kim, Two-dimensional photonic band-gap defect mode Laser, Science 284 (1999), 1819–1821.
8. M. Florescu and S. John, Single-atom switching in photonic crystals, Phys Rev A 64 (2001), 033801-1–033801-21.
9. I. El-Kady, W.W. Chow, and J.G. Fleming, Emission from an active photonic crystal, Phys Rev B 72 (2005), 195110–1–195110–5.
10. H. Xin, Z. Wu, A. Young, and R. Ziolkowski, THz thermal radiation enhancement using an electromagnetic crystal, IEEE Trans Antennas Propag 56 (2008), 2970–2980.
11. Z. Wu, A. Young, and H. Xin, Investigation of Terahertz (THz) electromagnetic band gap structures, ID 5914, In: Asia Pacific Microwave Conference, Hong Kong, China, 2008.
12. S.Y. Lin, J.G. Fleming, D.L. Hetherington, B.K. Smith, R. Biswas, K.M. Ho, M.M. Sigalas, W. Zubrzycki, S.R. Kurtz, and J. Bur, A three-dimensional photonic crystal operating at infrared wavelengths, Nature 394 (1998), 251–253.
13. S.G. Johnson and J.D. Joannopoulos, Block-iterative frequency-domain methods for Maxwell's equations in a planewave basis, Opt Express 8 (2001), 173–190.
14. A.R. Weily, K.P. Esselle, T.S. Bird, and B.C. Sanders, Experimental woodpile EBG waveguides, bends and power dividers at microwave frequencies, Electron Lett 42 (2006), 32–3-1–32–3-2.
15. J.G. Fleming, S.Y. Lin, I. El-Kady, R. Biswas, and K.M. Ho, All-metallic three-dimensional photonic crystals with a large infrared band gap, Nature 417 (2002), 52–55.
16. Ansoft Inc. Ansoft high frequency structure simulator, Ver. 10.1, Ansoft Inc., Pittsburg, PA.
17. A. Farjadpour, D. Roundy, A. Rodriguez, M. Ibanescu, P. Bermel, J.D. Joannopoulos, S.G. Johnson, and G. Burr, Improving accuracy by subpixel smoothing in FDTD, Opt Lett 31 (2006), 2972–2974.
18. J.B. Pendry, A.J. Holden, W.J. Stewart, and I.I. Youngs, Extremely low frequency plasmons in metallic mesostructures, Phys Rev Lett 76 (1996), 4773–4776.
19. M. Born and E. Wolf, Principles of optics: Electromagnetic theory of propagation, interference and diffraction of light, Pergamon Press, Oxford, 1964.
20. B. Martinez, I. Ederra, R. Gonzalo, B. Alderman, L. Azcona, P.G. Huggard, B.D. Hon, A. Hussain, S.R. Andrews, L. Marchand, and P. de Maagt, Manufacturing tolerance analysis, fabrication, and characterization of 3-D submillimeter-wave electromagnetic-band gap crystals, IEEE Trans Microwave Theory Tech 55 (2007), 672–681.
21. R. Gonzalo, B. Martinez, C.M. Mann, H. Pellemans, P.H. Bolivar, and P. de Maagt, A low-cost fabrication technique for symmetrical and asymmetrical layer-by-layer photonic crystals at submillimeter-wave frequencies, IEEE Trans Microwave Theory Tech 50 (2002), 2384–2392.
22. E. Öbay, E. Michel, G. Tuttle, R. Biswas, K.M. Ho, J. Bostak, and D.M. Bloom, Terahertz spectroscopy of three-dimensional photonic bandgap crystals, Opt Lett 10 (1994), 1155–1157.
23. F. Laermer and A. Urban, Challenges, developments and applications of silicon deep reactive ion etching, Microelectron Eng 67–68 (2003), 349–355.
24. G. Kiriakidis and N. Katsarakis, Fabrication of 2-D and 3-D photonic band-gap crystals in the GHz and THz regions, Mater Phys Mech 1 (2000), 20–26.
25. B.S. Liu, X. Gong, and W.J. Chappell, Applications of layer-by-layer polymer stereolithography for three-dimensional high-frequency components, IEEE Trans Microwave Theory Tech 52 (2004), 2567–2575.
26. K.F. Brakora, J. Halloran, and K. Sarabandi, Design of 3-D monolithic MMW antennas using ceramic stereolithography, IEEE Trans Antenn Propag 55 (2007), 790–797.
27. V.K. Varadan, X. Jiang, and V.V. Varadan, Microstereolithography and other fabrication techniques for 3D MEMS, Wiley, Chichester, UK, 2001.
28. N. Delhote, D. Baillargeat, S. Verdeyme, M. Thevenot, C. Delage, and C. Chaput, Large experimental bandpass waveguide in 3D EBG woodpile manufactured by layer-by-layer ceramic stereolithography, In: IEEE MTT-S Int Microwave Symp, Honolulu, Hawaii, 2007, pp. 1431–1434.
29. N. Delhote, D. Baillargeat, S. Verdeyme, C. Delage, and C. Chaput, Ceramic layer-by-layer stereolithography for the manufacturing

of 3-D millimeter-wave filters, IEEE Trans Microwave Theory Tech 55 (2007), 548–554.
30. Z. Wu, J. Kinast, M.E. Gehm, and H. Xin, Rapid and inexpensive fabrication of Terahertz electromagnetic bandgap structures, Opt Express 21 (2008), 16442–16451.
31. S.G. Johnson and J.D. Joannopoulos, Three-dimensionally periodic dielectric layered structure with omnidirectional photonic band gap, Appl Phys Lett 77 (2000), 3490–3492.
32. M. Qi, E. Lidorikis, P.T. Rakich, S.G. Johnson, J.D. Joannopoulos, E.P. Ippen, and H.I. Smith, A three-dimensional optical photonic crystal with designed point defects, Nature 429 (2004), 538–542.
33. G. Gruner, Millimeter and submillimeter wave spectroscopy of solids, Springer, Berlin, 1998.
34. P.Y. Han, M. Tani, M. Usami, S. Kono, R. Kersting, and X.C. Zhang, A direct comparison between terahertz time-domain spectroscopy and far-infrared Fourier transform spectroscopy, J Appl Phys 89 (2001), 2357 1–3.

© 2010 Wiley Periodicals, Inc.

A NOVEL HYBRID PLANAR SIW MAGIC TEE AND MONOPULSE ANTENNA

Minggang Liu and Zhenghe Feng
State Key Lab on Microwave and Digital Communications, Department of Electronic Engineering, Tsinghua University, Beijing 100084, People's Republic of China; Corresponding author: lmg03@mails.tsinghua.edu.cn

Received 20 August 2009

ABSTRACT: *In this article, a novel planar substrate integrated waveguide (SIW) magic Tee is proposed, and the magic Tee is implemented in a monopulse antenna design. Although the E arm is lain down, the magic Tee is of good performance. The magic Tee is used in a monopulse SIW slot array, and the beam pattern is measured.* © 2010 Wiley Periodicals, Inc. Microwave Opt Technol Lett 52: 686–689, 2010; Published online in Wiley InterScience (www.interscience.wiley.com). DOI 10.1002/mop.24990

Key words: *magic Tee; SIW; planar; slot array; monopulse antenna*

1. INTRODUCTION

Substrate integrated waveguide (SIW) technology has been proposed for many years [1, 2]. Because of the advantages of this technology, such as low cost, high Q-factor, low insertion loss, easy to be integrated, and high density layout, SIW is widely used in many areas, for example, planar slot antenna array [3, 4], filter [5], diplexer, hybrid coupler, power splitter, and so on. In the article ''A Novel Hybrid Planar SIW Magic Tee'' [6], which has been published in APMC2008, an SIW magic Tee is proposed. In the article, the magic Tee is implemented in a design of monopulse antenna. The monopulse antenna is based on the SIW slot array, which was published in ICMMT2008 [7]. The H Tees in the feeding network of the original SIW slot array is replaced by the SIW magic Tees of the new designed monopulse antenna. The pattern of the monopulse antenna is shown in this article too.

2. THE MAGIC TEE

Figure 1 shows the 3D structure of the planar SIW magic Tee, and the four ports of it are marked. The magic Tee is based on a SIW H Tee, and the E arm over is laid down, which is a SIW terminated by short-circuit. The magic Tee is of double layer, and the thicknesses of each dielectric substrate is 2 mm, with relative permittivity $\varepsilon_r = 2.25$. The center frequency of this magic Tee is 5.7 GHz.

The E arm couples to the H Tee by a slot in the middle. In either the E arm or the H arm, there is a pair of metal posts for matching. The dimensions could be referred to [6].

Because the E arm is lain down in this design, there are some essential differences between this planar magic Tee and the traditional one.

First, the short-circuit terminal of the E arm is placed $\lambda_g/2$, about 27 mm, away from the coupling slot. This structure functions as a balun. Because of the symmetrical structure of traditional magic Tee, the collinear arms are excited balanced by the E arm, but when E arm is lain down, the structure is no longer symmetrical, and a balun is needed.

Second, the E arm is not right above the collinear arms. There is a metal post right in the middle of the Tee junction, which could help match the H arm. However, the post is not placed below the coupling slot as traditional metal magic Tee, otherwise the post would not be able to connect the upper and lower walls of the H Tee junction and have no effect for matching.

Third, the width of H arm is 4 mm wider at the vicinity of the Tee junction as shown in Figure 1. Because the coupling slot is shifted form the junction into H arm, the coupling between E arm and collinear arms becomes weak. When the H arm is widened, more EM wave transmits from coupling slot to collinear arms.

To measure the SIW magic Tee, special waveguide-coaxial converters are designed and the test scheme is shown in Figure 2. One waveguide-coaxial converter is connected to the port of the E arm on the top, and three other converters are connected to the three ports of the H Tee below. The measured results in Figure 3 show the good performance of the planar SIW magic Tee in the desired frequency range 5.6–5.9 GHz. All ports are well matched and the return losses are below −20 dB [Fig. 3(a)]. The insertion loss of transmission coefficients of both E Tee and H Tee is about 0.2–0.8 dB. The isolation [Fig. 3(d)] between collinear arms is below −22 dB, and the isolation between E arm and H arm is much better, below −32 dB.

3. THE MONOPULSE ANTENNA

Monopulse antenna is based on the planar magic Tee and an SIW planar slot antenna array with chokes [7]. The antenna consists of two dielectric substrates. The top substrate is radiation waveguides with slots and bottom substrate is the feeding and

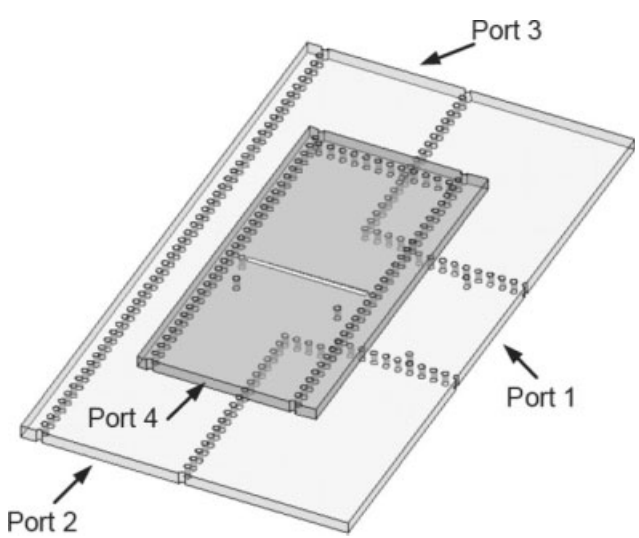

Figure 1 3D structure of the planar magic Tee